Simultaneous design of the topology and the build orientation of Wire-and-Arc Additively Manufactured structural elements

Matteo Bruggi[a], Vittoria Laghi[b,], Tomaso Trombetti[b]

[a]*Department of Civil and Environmental Engineering, Politecnico di Milano, 20133, Milano, Italy*
[b]*Department of Civil, Chemical, Environmental and Materials Engineering, University of Bologna, 40136, Bologna, Italy*

Abstract

Wire-and-Arc Additive Manufacturing (WAAM) has been recently adopted to create innovative structural forms and architectural shapes. As shown by a few experimental investigations, the layer-by-layer deposition induces a remarkable anisotropy in the elastic response of the WAAM-produced alloys. A suitable topology optimization technique is implemented to account for this peculiar behavior of the material, which is generally disregarded in design tools that are conceived for traditional manufacturing. First, an orthotropic material model is derived from the data of an experimental investigation that was recently performed on alloys made with 308LSi stainless steel wire feed. Then, an optimization procedure is implemented that exploits, as design variables, not only the density field of an orthotropic material phase, but also the orientation of the symmetry axes of such a material with respect to a reference frame (i.e. the printing direction used to build the whole structural element). Minimum weight problems with displacement constraints are solved to find optimal solutions that are compared to those achieved by performing topology optimization with (i) isotropic stainless steel or with (ii) the WAAM-produced alloy for prescribed orientations. Numerical simulations assess that the printing direction remarkably affects the stiffness of the

---

Email addresses: `matteo.bruggi@polimi.it` (Matteo Bruggi), `vittoria.laghi2@unibo.it` (Vittoria Laghi), `tomaso.trombetti@unibo.it` (Tomaso Trombetti)

optimal layouts, as well as their topology.

1. Introduction

Along the centuries, the evolution in building construction has always been strictly linked to significant advancements in material science, technology, industrial processes and engineering [1]. During the last 30 years, the way structures have been designed, planned and built changed completely with the technological innovations offered by software for Computer-Aided Design (CAD). This replaced manual drawings, without however, at the beginning, changing the resulting architectural shapes.

In the early years of the 21st century, a new design approach in architecture started to emerge resulting in novel forms thanks to the introduction of three-dimensional computer modelling and digital fabrication methods. More recently, with the advent of the "digital turn" [2], novel computerized tools for architecture, structural and civil engineering have gained influence, enabling the design and construction of buildings with complex, doubly-curved geometry, such as shell structures and other free-form designs, see e.g. [3, 4].

Additive Manufacturing (AM)-based technologies are already commonly used in other sectors such as aerospace, automotive and biomedical engineering, see e.g. [5, 6]. In the last few years, the fast development in digital fabrication techniques is leading towards applications also in the field of structural engineering. Among the different AM processes, the Wire-and-Arc Additive Manufacturing (WAAM) technology, which consists of standard welding equipment mounted on top of a numerically-controlled robotic arm, allows for a relatively fast realization of members of large dimensions (up to few meters span). For such reason, it results to be the most suitable technique for civil engineering and construction applications to realize innovative architectural

forms, with ideally almost no limitations in size or shape, see in particular [7–9].

Recent investigations on the microstructural and mechanical characterization of WAAM stainless steel members revealed the anisotropic nature of the material peculiar to the layer-by-layer deposition process. Different mechanical properties of the material are reported along different directions, in terms of both Young's modulus and strength [10–18].

Topology optimization (TO) [19] is a powerful design tool to sketch lightweight structural components, see also [20]. TO distributes a prescribed amount of material with the goal of minimizing an objective function, given a set of constraints. The design variable is the point-wise "density" of the material that takes values in the range $]0, 1]$ to affect the elastic properties of the material through a suitable interpolation law. To achieve pure 0-1 solutions, i.e. structures made by "full material" and "void", the so-called Solid Isotropic Model with Penalization (SIMP) can be used, see e.g. [21, 22]. The SIMP is a power law interpolation of the elastic modulus that remarkably penalizes intermediate densities of the material.

Lots of efforts are being made by the scientific community towards AM and TO to leverage the full potential of their combined use. For an overview of recent trends and developments, reference is made to review papers such as [23] and [24].

In many approaches of topology optimization for additive manufacturing, the build direction is mainly addressed with respect to possible overhang issues. In a layer-by-layer printing process, when the upper layer is not entirely supported by the lower one, additional supports may be requested to sustain overhangs and bridges. Reference is made e.g. to [25] and [26] for the optimal design of supports in layer-by-layer fabrication process, and to [27] and [28] for stage-dependent approaches of topology optimization. In general, the build orientation is set a-priori in a topology optimization problem. In the work by [29] and [30] simultaneous part and orientation optimization is performed to achieve optimal layouts that are self-supporting or need for limited amount of support. The recent contribution by [31] explores flexible fabrication beyond planar

layer-by-layer deposition, by investigating the concurrent optimal design of a structure and its fabrication sequence.

In this work, the build orientation is taken into account with respect to the anisotropy affecting the mechanical response of the printed material.

It must be remarked that the mechanical implications of the material orientation are of primary importance in special classes of optimization problems. This is the case e.g. of topology optimization with oriented periodic microstructures, see in particular [32] and [33], and of composite optimization [34]. Among the others, the work in [36] addresses the simultaneous design of density and orientation of anisotropic material supporting both continuous and discrete orientation design. In [37] the topology and the fiber angle distribution of two-dimensional composite structures are simultaneously optimized, also showing that different optimal shapes arise in case of quasi-isotropic material and composite laminate. The work in [38] investigates the optimal distribution and orientation of the fiber-reinforcement to strengthen plates adopting a SIMP-based approach, whereas the contribution in [39] presents an effective formulation for stress-constrained topology optimization using layer-wise theory for composite laminates, see also [40]. The recent work in [41] performs concurrent optimization of spatial distribution and material orientation, by writing the compliance tensor of orthotropic two-dimensional media in terms of polar invariants [42] and performing a double minimization of the complementary energy. In all the above mentioned approaches, the orientation of the material is an unknown field. Indeed, it can take different values within the part.

In this work WAAM is addressed focusing on a layer-by-layer manufacturing process that adopts the same build orientation within the part. Indeed, the WAAM process commonly adopts a constant build orientation in the fabrication of the same part, with the aim of achieving high quality of the outcomes [15]. At first, based on some recent experimental tests on alloys produced with 308LSi stainless steel wire feed, a suitable orthotropic material model is derived. Then, a

displacement-constrained minimum weight formulation is presented that adopts as design variables not only the density field, but also the printing direction, i.e. the angle between the symmetry axes of the orthotropic alloy and the axes of the reference system of the part. The arising optimization problem is solved through sequential convex programming. The adjoint method is used to compute sensitivity with respect to the unknowns in an efficient way.

Numerical simulations are presented to show that the build orientation remarkably affects the shape and the stiffness of the achieved optimal design. Comparisons with optimal layouts achieved in the case of isotropic steel and orthotropic alloys with given orientation are addressed as well.

The paper is organized as follows. Section 2 is devoted to the Wire-and-Arc Additively Manufactured material. Section 2.1 reports the experimental results that are used in Section 2.2 to address the orthotropic modeling of the printed material. The simultaneous design of topology and build orientation within a displacement-constrained minimum weight problem is addressed in Section 3. Section 4 presents numerical simulations, whereas Section 5 concerns conclusions and ongoing research.

2. The Wire-and-Arc Additively Manufactured material

Wire-and-Arc Additive Manufacturing consists of an electric arc as heat source and metal wire as feed. The process is usually realized through a numerically-controlled robotic arm with a velocity of 2 to 10 kg/hour. The printed outcome of a WAAM process is typically a planar geometry created through the deposition of successive layers of welding metal. Thus, the element is characterized by two main directions: one along the deposited layer (longitudinal direction) and one perpendicular to it (transversal direction).

2.1. Experimental investigation

Several experimental studies focused on the possible anisotropic behavior of WAAM-produced elements [13–18]. First, the deposition of successive layers results in a non-uniform geometry
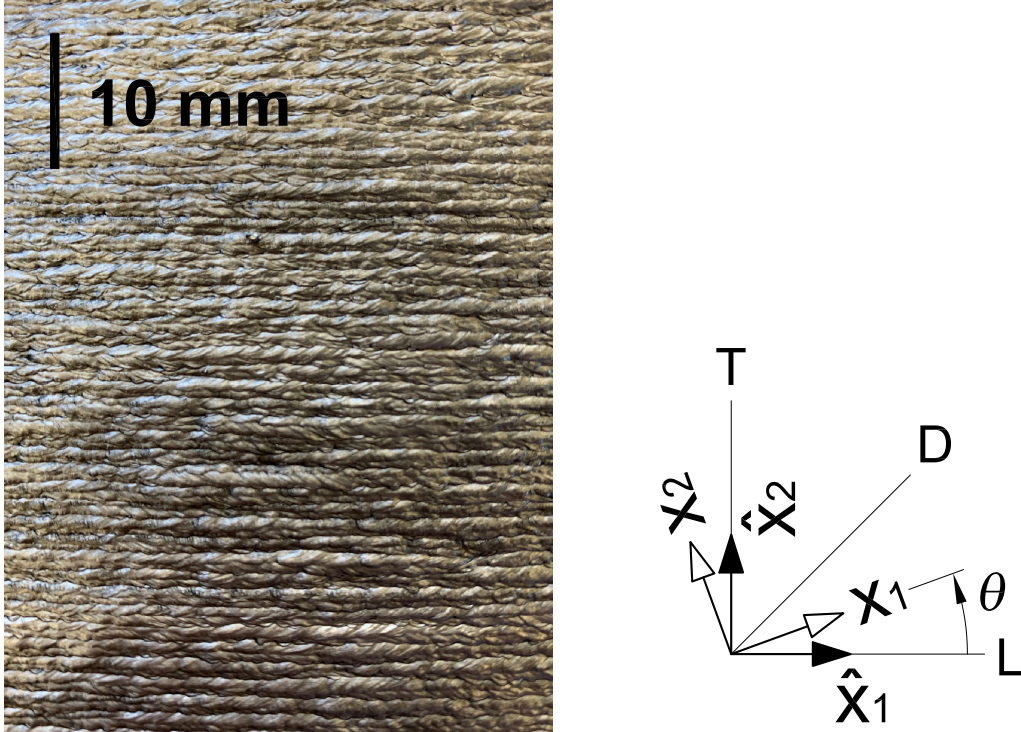
Figure 1: As built WAAM-produced stainless steel plate [16, 18, 43]. The longitudinal direction (L), i.e. the direction of the printed layers, corresponds to the horizontal direction in this picture.

and surface, thus providing an inherent surface roughness and non-negligible discrepancy of the real geometrical shape with the nominal one [16, 18, 43]. Moreover, the microstructural analysis proved that the deposition layers induce an anisotropic microstructure, see e.g. [12]. This affects the mechanical response of the members, so that the apparent stiffness and strength depends on the direction of the applied load.

Recently, some of the authors carried out a wide experimental investigation at University of Bologna labs aimed at characterizing the WAAM-produced stainless steel material for structural engineering applications. In detail, a series of experimental tests on planar specimens realized with 308LSi stainless steel wire feed has been developed. From the geometrical point of view,
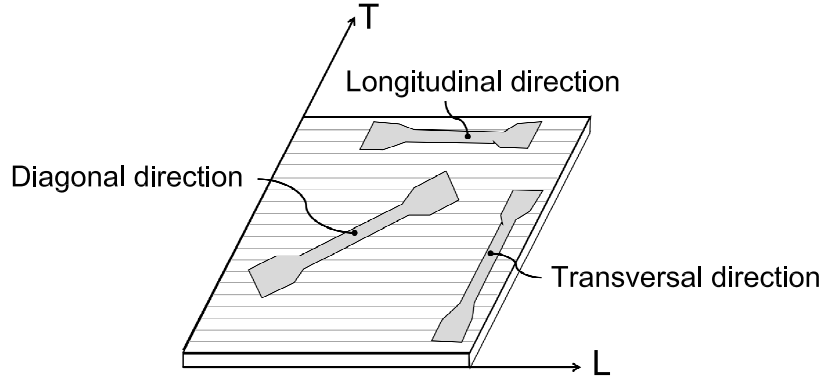
Figure 2: Dog-bone specimes cut from the as-built WAAM-produced plate [16, 18, 43].

volume-based measurements and 3D scanning acquisitions have been performed, to study the surface roughness and distribution of thickness variation along the specimens with reference to the random process theory [18]. Figure 1 shows the typical surface roughness of the as-built planar elements, which are plates with nominal (average) thickness 4 mm. Then, further studies focused on the mechanical response of the material have been performed. To this aim, dog-bone specimens were obtained by cutting samples from the as-built plate along the longitudinal direction (L), the transversal direction (T) and a diagonal direction (D) that is inclined of 45° with respect to the previous ones, see Figure 2. Samples were subsequently polished by means of mechanical milling, to achieve uniform cross-section throughout each specimen, see Figure 3. Tensile tests were performed to compute the Young's modulus (E), the 0.2% proof stress ($R_{p,02}$), the ultimate tensile strength (UTS) and the elongation at rupture ($A_{\%}$). For specimens L and T, the transversal elastic strain was also measured to compute the ratio to the longitudinal strain in the elastic loading direction, i.e. to derive the Poisson's ratio ν. Mean values and standard deviations of the key mechanical parameters along the longitudinal (L) transversal (T) and diagonal (D) directions are reported in Table 1 for the WAAM material, along with mean values for Grade 304L stainless steel according

7

Material	E [GPa]	$R_{p,02}$ [MPa]	UTS [MPa]	ν [-]
WAAM-L	135.84 ± 15.42	340.67 ± 20.21	567.39 ± 17.12	0.46 ± 0.07
WAAM-T	106.09 ± 2.98	352.54 ± 18.36	552.53 ± 48.30	0.38 ± 0.04
WAAM-D	243.09 ± 32.79	412.90 ± 39.33	604.81 ± 61.68	-
Grade 304L	200	$190 \div 230$	$500 \div 540$	0.3

Table 1: Key material properties of WAAM-produced stainless steel [17, 18] vs. Grade 304L stainless steel [44].

to Eurocode 3 provisions [44]. Indeed, this is adopted as the reference isotropic material to address conventional subtractive manufacturing in the following simulations.

In order to further compare the different orientations, Figure 4 shows through histograms mean values and deviations of the material properties for directions L, T and D with reference to Grade 304L.

The ultimate tensile strength of WAAM material is not very sensitive to the specimens orientation, being the gap between the maximum and minimum values observed in the experiments around 6%. Both values are slightly bigger than those of the conventional interval given for the reference steel. Referring to the 0.2% proof stress of WAAM specimens, the minimum value among the tests is found in the longitudinal direction, whereas the maximum one arises in the diagonal direction (about +20%). With respect to the reference stainless steel, the offset yield point of WAAM material occurs at remarkably higher stress values, regardless the specimens orientation. In terms of Young's modulus, the lowest value of the tested WAAM specimens is found for the transversal direction, whereas the maximum one arises in the diagonal one (about +130%). Looking at both longitudinal and transversal directions, WAAM material is much more flexible than the conventional steel, while it is approximately 20% stiffer in the diagonal direction.

Hence, a remarkable influence on the orientation arises in terms of stiffness, while tensile strength is less affected by the specimens orientation. In the following sections, the characterization of the material will focus on the former issue.

Figure 3: Surface roughness of the dog-bone specimens: as cut from the as-built plate (a), after surface milling (b) [16, 18, 43].

Microstructural features of the WAAM-produced stainless steel referenced above were originally investigated in [17]. The as-built samples were found to be substantially defect-free and characterized by a fully dense material. The microstructural characterization performed in [17] pointed out a hierarchical microstructure, consisting in deposition layers, columnar grains crossing over layers, and a fine cellular sub-structure within the grains. The columnar grains and the fine cellular sub-structure share the same orientation, i.e. they are perpendicular to the deposition layer. The very good properties in terms of 0.2% proof stress, ultimate tensile strength and Young's modulus observed in the diagonal direction are mainly related to the crystallographic and mechanical fibering induced by the AM process. In the tensile testing of dog-bone samples, the preferential slip direction for plastic deformation is oriented at 45° with respect to the main axis
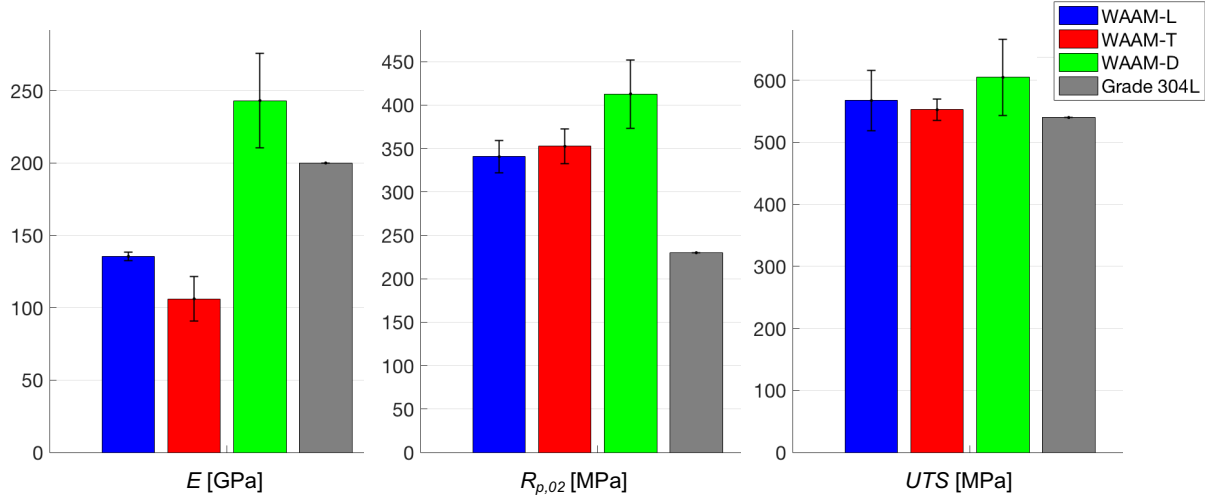
9

Figure 4: Overview of the key material properties of WAAM-produced stainless steel [17, 18] vs. Grade 304L stainless steel [44].

of the specimen. For samples cut along the diagonal direction (D), a very high density of cell boundaries is reported along this orientation, thus providing an effective obstacle to the arising of plastic deformations. Reference is also made to [12] and [45] for further insight on the relationship between microstructural evolution and tensile properties in WAAM-produced steel.

2.2. Orthotropic plane stress modeling

The material symmetries of the plates created through the WAAM technique, see Figure 1, suggest the adoption of an orthotropic plane stress material model. The symmetry axes of the orthotropic medium are denoted as $\widehat{x}_1$ and $\widehat{x}_2$, i.e. the printing direction (L) and the transversal direction (T), respectively. In the material reference system $O\widehat{x}_1\widehat{x}_2$, the components of the stress tensor are re-gathered in the array $\widehat{\boldsymbol{\sigma}} = [\widehat{\sigma}_{11}\,\widehat{\sigma}_{22}\,\widehat{\sigma}_{12}]^T$ and, equally, $\widehat{\boldsymbol{\varepsilon}} = [\widehat{\varepsilon}_{11}\,\widehat{\varepsilon}_{22}\,\widehat{\varepsilon}_{12}]^T$ for the

10

components of the strain tensor. Hence, $\widehat{\boldsymbol{\varepsilon}} = \widehat{\boldsymbol{C}}\,\widehat{\boldsymbol{\sigma}}$, where the compliance matrix reads:

$$
\widehat{\mathbf{C}} = \begin{bmatrix} 1/\widehat{E}_1 & -\widehat{\nu}_{21}/\widehat{E}_2 & 0 \\ -\widehat{\nu}_{12}/\widehat{E}_1 & 1/\widehat{E}_2 & 0 \\ 0 & 0 & 1/\widehat{G}_{12} \end{bmatrix}.
\tag{1}
$$

In Eqn. (1) $\widehat{E}_1, \widehat{E}_2$ are the Young's moduli of the material along $\widehat{x}_1$ and $\widehat{x}_2$, respectively, $\widehat{G}_{12}$ is the in-plane shear modulus and $\widehat{\nu}_{12}, \widehat{\nu}_{21}$ are Poisson's ratios ($\widehat{\nu}_{ij} > 0$ corresponds to a contraction in direction $\widehat{x}_j$ when an extension is applied in direction $\widehat{x}_i$). The equality $\widehat{\nu}_{12}\widehat{E}_2 = \widehat{\nu}_{21}\widehat{E}_1$ holds.

A general reference system Ox_1x_2 is defined, denoting by θ the counterclockwise rotation of the axis x_1 with respect to $\widehat{x}_1$. The stress-strain law in the global reference system reads $\boldsymbol{\varepsilon} = \boldsymbol{C}\,\boldsymbol{\sigma}$, being $\boldsymbol{\sigma} = [\sigma_{11}\,\sigma_{22}\,\sigma_{12}]$ and by $\boldsymbol{\varepsilon} = [\varepsilon_{11}\,\varepsilon_{22}\,2\varepsilon_{12}]$ the stress and strain components, respectively, as written in Ox_1x_2. The compliance matrix reads:

$$
\boldsymbol{C} = \boldsymbol{T}_\varepsilon(\theta)\,\widehat{\boldsymbol{C}}\,\boldsymbol{T}_\sigma^{-1}(\theta) = \boldsymbol{T}_\varepsilon(\theta)\,\widehat{\boldsymbol{C}}\,\boldsymbol{T}_\varepsilon^T(\theta),
\tag{2}
$$

where the transformation matrix for the strain tensor and the stress tensor may be computed as:

$$
\mathbf{T}_\varepsilon(\theta) = \begin{bmatrix} c^2 & s^2 & cs \\ s^2 & c^2 & -cs \\ -2cs & 2cs & c^2 - s^2 \end{bmatrix}, \quad \mathbf{T}_\sigma(\theta) = \begin{bmatrix} c^2 & s^2 & 2cs \\ s^2 & c^2 & -2cs \\ -cs & cs & c^2 - s^2 \end{bmatrix},
\tag{3}
$$

respectively, being $c = \cos\theta$ and $s = \sin\theta$ for brevity. It is recalled that $\boldsymbol{\varepsilon} = \boldsymbol{T}_\varepsilon\widehat{\boldsymbol{\varepsilon}}$, $\boldsymbol{\sigma} = \boldsymbol{T}_\sigma\widehat{\boldsymbol{\sigma}}$ and $\boldsymbol{T}_\sigma^T\boldsymbol{T}_\varepsilon = \boldsymbol{I}$ holds, see e.g. [46] and [47]. According to Eqn. (2), the inverse of the apparent elastic modulus in the direction x_1 reads:

$$
1/E_1 = c^2\left(c^2 - \widehat{\nu}_{12}s^2\right)/\widehat{E}_1 + s^2\left(s^2 - \widehat{\nu}_{21}c^2\right)/\widehat{E}_2 + c^2 s^2/\widehat{G}_{12},
\tag{4}
$$

see $C(1,1)$, whereas the inverse of the apparent shear modulus referring to axes x_1 and x_2 reads:

$$1/G_1 = (c^2 - s^2)^2/\widehat{G}_{12} + 4c^2s^2 \left(1 + \widehat{\nu}_{12}\right)/\widehat{E}_1 + 4c^2s^2 \left(1 + \widehat{\nu}_{21}\right)/\widehat{E}_2, \tag{5}$$

see $C(3,3)$.

Four elastic constants are needed to fully characterize the elastic response of the WAAM material through Eqn. (1). The Young's moduli along $\widehat{x}_1$ and $\widehat{x}_2$ are assumed equal to the relevant mean values derived from the experimental investigation, i.e. $\widehat{E}_1 = 135.84\,\text{GPa}$ and $\widehat{E}_2 = 106.09\,\text{GPa}$. The following minimization problem is considered to select $\widehat{\nu}_{12}$ and $\widehat{\nu}_{12}$ such that symmetry of $\boldsymbol{C}$ is met:

$$\begin{cases} \min_{\widehat{\nu}_{12},\widehat{\nu}_{21}} & \left(\widehat{\nu}_{12} - \nu_{LT}\right)^2 + \left(\widehat{\nu}_{21} - \nu_{TL}\right)^2 \\ \text{s.t.} & \widehat{\nu}_{12}\widehat{E}_2 = \widehat{\nu}_{21}\widehat{E}_1, \end{cases} \tag{6}$$

where ν_{LT} and ν_{TL} are the mean values of the Poisson's ratios evaluated through experiments in the longitudinal and in the transversal direction, respectively, see Table 1. Thus:

$$\widehat{\nu}_{12} = \frac{\widehat{E}_1}{\widehat{E}_1 + \widehat{E}_2}(\nu_{LT} + \nu_{TL}) = 0.47, \qquad \widehat{\nu}_{21} = \frac{\widehat{E}_2}{\widehat{E}_1 + \widehat{E}_2}(\nu_{LT} + \nu_{TL}) = 0.37, \tag{7}$$

which are no more than 0.01 above or below the relevant experimental mean values. Finally, recalling that the mean value of the apparent Young's modulus in the diagonal direction E_D is known from the experimental investigation, the shear modulus $\widehat{G}_{12}$ can be found by evaluating Eqn. (4) for $\theta = 45°$. Therefore:

$$\widehat{G}_{12} = \left(\frac{4}{E_D} - \frac{1 - \widehat{\nu}_{12}}{\widehat{E}_1} - \frac{1 - \widehat{\nu}_{21}}{\widehat{E}_2}\right)^{-1} = 151.25\,\text{GPa}. \tag{8}$$

The compliance matrices used in the simulations to handle the WAAM-produced stainless steel and the Grade 304L stainless steel are:

$$\widehat{\mathbf{C}}_{w,0} = \begin{bmatrix} 0.0074 & -0.0035 & 0 \\ -0.0035 & 0.0094 & 0 \\ 0 & 0 & 0.0066 \end{bmatrix}, \tag{9a}$$

$$\mathbf{C}_{s,0} = \begin{bmatrix} 0.0050 & -0.0015 & 0 \\ -0.0015 & 0.0050 & 0 \\ 0 & 0 & 0.0130 \end{bmatrix}, \tag{9b}$$

respectively. $\widehat{\mathbf{C}}_{w,0}$ is written in the material reference system, $\mathbf{C}_{s,0}$ in the general reference system and units are GPa^{-1}.

Figure 5 shows polar diagrams of the apparent Young's modulus and shear modulus of the WAAM-produced stainless steel, as computed through Eqn. (4) and (5), respectively. Those of the isotropic Grade 304 stainless steel are shown for comparison. The orientation θ is measured from $\widehat{x}_1$. The minimum value of the apparent Young's modulus is along the transversal direction, i.e. $E_{min} = 106.09\,\mathrm{GPa}$, whereas the maximum one $E_{max} = 246.82\,\mathrm{GPa}$ is found for $\pm 41.5°$. $E_{min} < E_s$, but $E_{max} > E_s$, being E_s the elastic modulus of Grade 304 stainless steel. The minimum value of the apparent shear modulus $G_{min} = 42.14\,\mathrm{GPa}$ arises when the axes are rotated of $\pm 45°$ with respect to the material reference system, whereas the maximum value $G_{max} = 151.25\,\mathrm{GPa}$ is found when the axes lie along the longitudinal and transversal directions. It is also remarked that any normal stress exerted along one of the symmetry axes of the material generates axial strains only; when arbitrary directions are considered, both axial and shear strains are expected.
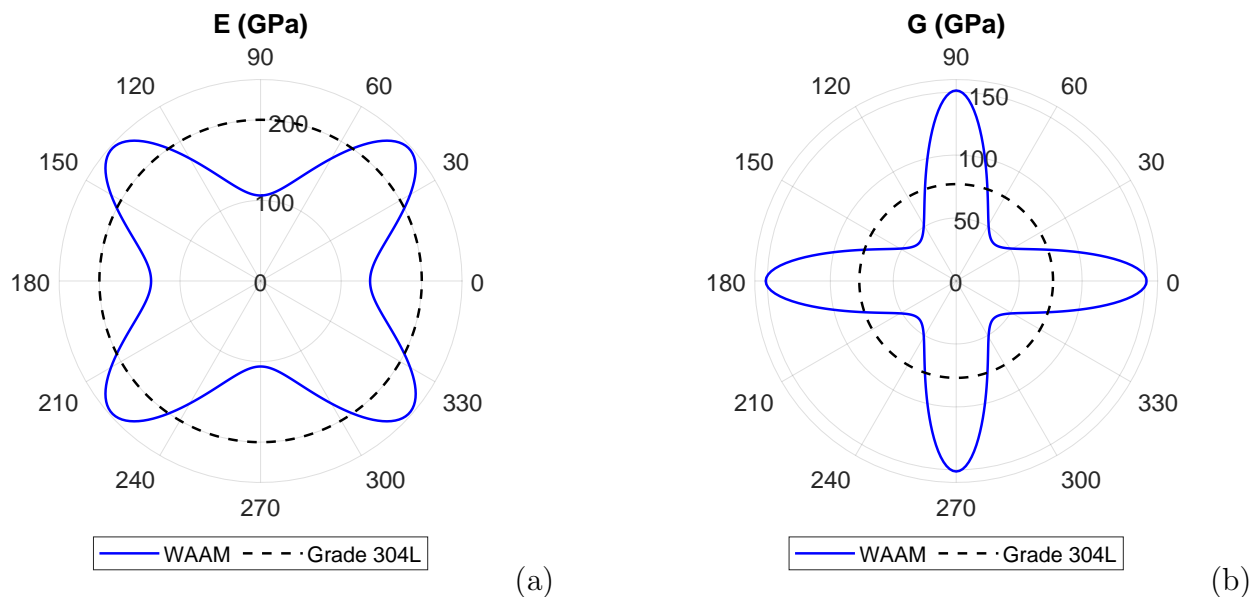
Figure 5: Polar plots of the Young's modulus (a) and shear modulus (b) of WAAM-produced stainless steel and of Grade 304 stainless steel. The angular coordinate identifies the direction along which the value is given with respect to $\widehat{x}_1$.

3. Simultaneous design of topology and orientation for minimum weight under displacement constraint

The design of two dimensional structural elements for WAAM is herein formulated as a displacement-constrained minimum weight problem.

In the numerical simulations presented in Section 4, the controlled displacement is that at the loaded point along the direction of the applied force. The scalar product of the controlled displacement and the applied force provides the work of the external load at equilibrium, i.e. the compliance. Hence, the proposed problem is a compliance-constrained minimum weight problem, which is in turn equivalent to a classical weight-constrained minimum compliance problem. The same solution (up to a scaling) is expected to arise when considering either problem, see in particular [35], meaning that both formulations can be used to investigate the lightweight design of

14

stiff structural elements.

The text that follows describes the formulation for the simultaneous design of topology and orientation of the material. The numerical simulations presented in Section 4 include simulations performed for different sets of prescribed orientations. A displacement-constrained formulation allows investigating optimal layouts by enforcing requirements at the serviceability limit state. The amount of material needed to meet this requirement is an outcome of the problem. This is used to perform comparisons when different assumptions are made concerning the modeling/orientation of the WAAM-produced material for the same example.

A finite element discretization of a given design domain is operated, employing standard four-node displacement-based elements. A set of element-wise discrete design variables is considered. In the e-th of the n elements of the mesh, $0 < \rho_e \leq 1$ is a variable that controls the "density" of the orthotropic material. Additionally, the variable θ, see Section 2.2, governs the orientation of the material. It remains the same throughout the design domain because it is assumed that the printing direction does not change during the fabrication process. The range $0 \leq \theta < 180°$ is used for the side constraints of this variable, see Figure 5. It must be remarked that θ governs the (counterclockwise) rotation of the axis x_1 of the general reference system with respect to the axis $\widehat{x}_1$ of the material reference system. Assuming that the design domain is described in the general reference system Ox_1x_2, the orientation of the printed layers with respect to the axis x_1 is given by a (counterclockwise) rotation of this axis equal to $\alpha = 180° - \theta$, see Figure 6.

The Solid Isotropic Material with Penalization (SIMP) extensively used in topology optimization [19] is modified to handle orthotropic media as follows, see in particular [36] and [48]. Due to the adopted finite element implementation, the direct form of the constitutive law is considered, i.e. $\boldsymbol{\sigma} = \boldsymbol{C}^{-1}\boldsymbol{\varepsilon}$. In the e-th element, the constitutive matrix $\boldsymbol{C}^{-1}(\rho_e, \theta)$ may be written as:

$$\boldsymbol{C}^{-1}(\rho_e, \theta) = \rho_e^p \; \boldsymbol{T}_\sigma(\theta) \, \widehat{\boldsymbol{C}}_{w,0}^{-1} \boldsymbol{T}_\varepsilon^{-1}(\theta) = \rho_e^p \; \boldsymbol{T}_\sigma(\theta) \, \widehat{\boldsymbol{C}}_{w,0}^{-1} \boldsymbol{T}_\sigma^T(\theta), \tag{10}$$
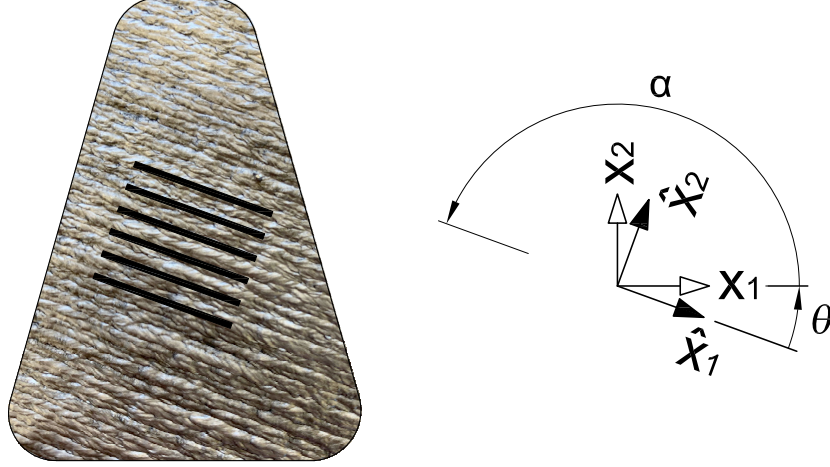
15

Figure 6: Orientation of the printed layers for an object described in the general reference system with axis x_1 and x_2 ($\alpha = 180° - \theta$).

where $\widehat{\boldsymbol{C}}_{w,0}^{-1}$ is the inverse of the compliance matrix of the WAAM material in the material reference system, see Eqn. (9a), and $p = 3$ is an interpolation parameter that penalizes intermediate densities.

A problem for the simultaneous design of topology and orientation of the WAAM material can be stated as:

$$
\begin{cases}
\displaystyle \min_{0<\rho_e\leq 1, 0\leq\theta<180°} \mathcal{W} = \sum_{e=1}^{n} \rho_e\, W_{0,e} & \text{(11a)} \\[2ex]
\text{s.t. } \mathbf{K}(\boldsymbol{\rho}, \theta)\, \mathbf{U} = \left(\sum_{e=1}^{n} \rho_e^p\, \mathbf{K}_{0,e}(\theta) \right) \mathbf{U} = \mathbf{F}, & \text{(11b)} \\[2ex]
u_a \leq u_{lim}. & \text{(11c)}
\end{cases}
$$

In the above statement, the objective function is the weight of the structural element, which is computed through the sum of the element contributions $\rho_e\, W_{0,e}$, being $W_{0,e}$ the weight of one

16

element for $\rho_e = 1$.

Eqn.(11b) prescribes the discrete equilibrium of the structural element. The global stiffness matrix $\mathbf{K}(\boldsymbol{\rho}, \theta)$ is computed by assembling the element contributions that account for the constitutive law given in Eqn.(10). The element stiffness matrix can be conveniently written as $\rho_e^p \mathbf{K}_{0,e}(\theta)$, where $\mathbf{K}_{0,e}(\theta)$ refers to $\rho_e = 1$. The load vector $\mathbf{F}$ allows computing the nodal displacement vector $\mathbf{U}$ under the effect of a given point load acting along x_1 or x_2. The scalar quantity u_a stands for the displacement computed at the loaded node in the direction of the applied force. It may be written as:

$$u_a = \mathbf{L}^T \mathbf{U}, \tag{12}$$

where $\mathbf{L}$ is a vector made of zeros except for the entry referring to the relevant displacement degree of freedom of the loaded node, which takes unitary value. Eqn.(11c) enforces a prescribed limit u_{lim} to u_a. $u_{lim} \geq u_0$ stands for the maximum displacement allowed at the serviceability limit state, where u_0 is the displacement computed for the design domain made of full material with layers oriented in the most favourable direction. Eqn. (11) can be used to explore lighter and lighter design by enforcing larger values of $u_{lim} \geq u_0$. This is equivalent to making an investigation by means of a volume-constrained minimum compliance problem with decreasing volume fraction (≤ 1).

3.1. Numerical implementation

For simplicity, a conventional linear filter [49, 50] is implemented on the element variables ρ_e to avoid potential issues that are well-known in topology optimization, i.e. the arising of mesh dependence and checkerboard patterns [21]. The original variables ρ_e are mapped to the new set

of $\tilde{\rho}_e$ as follows:

$$\tilde{\rho}_e = \frac{1}{\sum_n H_{eh}} \sum_n H_{eh} \, \rho_h, \tag{13a}$$

$$H_{eh} = \max(0, r_{min} - \text{dist}(e, h)), \tag{13b}$$

where $\text{dist}(e, h)$ is the distance between the centroid of the e-th and h-th element, and r_{min} is the filter radius. Maps of the filtered design variables $\tilde{\rho}_e$ are plotted in the numerical section, since they represent the physical "density" of the material in the elements. Alternative filtering schemes can be straightforwardly considered in the proposed procedure. Among the others, Heaviside projection techniques could be applied to the filtered density variables of Eqn.(13a) in order to achieve crisp black/white solutions, see in particular the formulation proposed in [51]. This calls for the adoption of a continuation approach, which means more iterations of the minimization algorithm to achieve convergence. Also, the nonlinear adaptive spatial filter introduced by [52] could be implemented to achieve layouts that fully comply with possible geometrical AM restrictions. This filter has been successfully tested in conjunction with the projection technique given in [51] to find print-ready solutions with black/white boundaries that do not require additional interpretation.

The optimization problem in Eqn. (11) is solved via mathematical programming, adopting the Method of Moving Asymptotes (MMA) [53] as minimizer. MMA is an iterative method. At each iteration, the minimizer provides the updated set of optimization unknowns, i.e. the current values of the element densities ρ_e and the value of the additional variable θ. A structured mesh using square finite elements is used to speed up the computation. Indeed, $\mathbf{K}_{0,e}(\theta)$ is computed only for one element at each iteration.

The adjoint method is used to compute sensitivity, see e.g. [21]. Accordingly, u_a in Eqn. (12) does not change when adding at the right hand side a zero function derived from the equilibrium

of Eqn.(11b), i.e.:

$$-\boldsymbol{\lambda}^T \left(\left(\sum_{e=1}^{n} \mathbf{K}_e(\rho_e, \theta) \right) \mathbf{U} - \mathbf{F} \right), \tag{14}$$

where $\boldsymbol{\lambda}$ is any arbitrary but fixed vector. After re-arrangement of terms, the derivative of u_a with respect to the j-th element unknown ρ_j and that with respect to the variable θ may be computed respectively as:

$$\frac{\partial u_a}{\partial \rho_j} = -\boldsymbol{\lambda}^T \frac{\partial \mathbf{K}(\boldsymbol{\rho}, \theta)}{\partial \rho_j} \mathbf{U}, \tag{15a}$$

$$\frac{\partial u_a}{\partial \theta} = -\boldsymbol{\lambda}^T \frac{\partial \mathbf{K}(\boldsymbol{\rho}, \theta)}{\partial \theta} \mathbf{U}, \tag{15b}$$

where $\boldsymbol{\lambda}$ satisfies the adjoint equation:

$$\left(\sum_{e=1}^{n} \mathbf{K}_e(\rho_e, \theta) \right) \boldsymbol{\lambda} = \left(\frac{\partial u_a}{\partial \mathbf{U}} \right)^T = \mathbf{L}. \tag{16}$$

Eqn. (15a) can be evaluated recalling that the derivative of the e-th element stiffness matrix with respect to ρ_j is equal to $p\rho_e^{p-1} \mathbf{K}_{0,e}(\theta)$. This sensitivity is null if $e \neq j$.

To compute Eqn. (15b), the derivative of Eqn.(10) with respect to the variable θ is required. It simply reads:

$$\frac{\partial \boldsymbol{C}^{-1}(\rho_e, \theta)}{\partial \theta} = 2\rho_e^p \, \frac{\partial \boldsymbol{T}_\sigma(\theta)}{\partial \theta} \, \widehat{\boldsymbol{C}}_{w,0}^{-1} \, \frac{\partial \boldsymbol{T}_\sigma^T(\theta)}{\partial \theta}. \tag{17}$$

The derivatives with respect to the filtered variables $\tilde{\rho}_e$ can be easily evaluated by applying the chain rule to Eqn. (13). It is also remarked that at each iteration of the minimization procedure only two linear systems are solved to evaluate constraints and their sensitivities, i.e. Eqn. (11b)
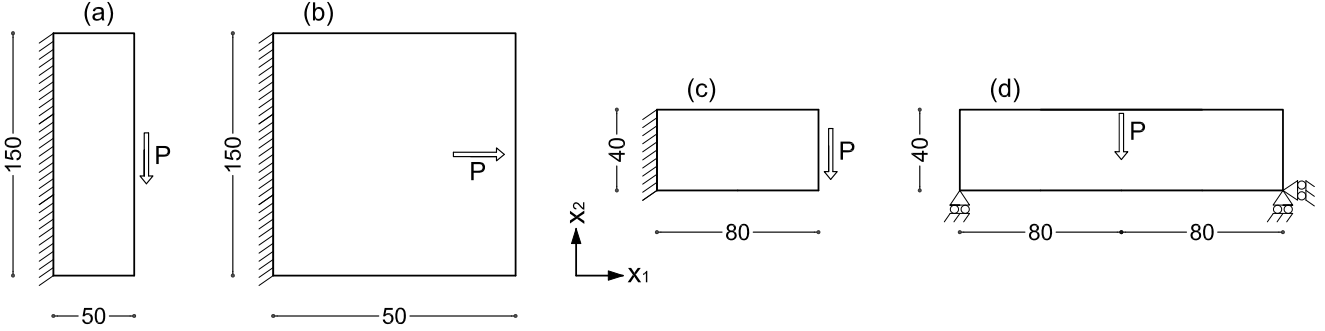
Figure 7: Geometry and boundary conditions for the numerical simulations. Dimensions are in cm.

and Eqn. (16). They share the same stiffness matrix.

4. Numerical simulations

A set of numerical simulations is presented, concerning the specimens depicted in Figure 7. For each one of the considered examples, the optimal design achieved in case of isotropic Grade 304L stainless steel is taken as a reference.

At first, optimal solutions using the orthotropic WAAM material are sought by prescribing the direction of the printed layers with respect to the horizontal axis x_1. Figure 8 provides polar plots of the Young's modulus of the WAAM-produced stainless steel for different values of the printing orientation, i.e. $\alpha = 0°, 90°$ (a) and $\alpha = 45°, 135°$ (b). In each diagram, the angular coordinate identifies the direction along which the apparent value of the elastic modulus is given with respect to x_1. The elastic modulus of the isotropic Grade 304 stainless steel is reported for comparison.

Then, the formulation in Eqn. (11) is applied to define, simultaneously, the topology of the material and the direction of the printing layers that gives the lightest solution.

The procedure is initialized with $\rho_e = 1, \forall e$. Iterations stop when the maximum relative change in the value of the discrete design variables is less than 10^{-3}. Due to the non-convexity of the problem, several starting points were considered to assess the achieved solutions. Indeed, different
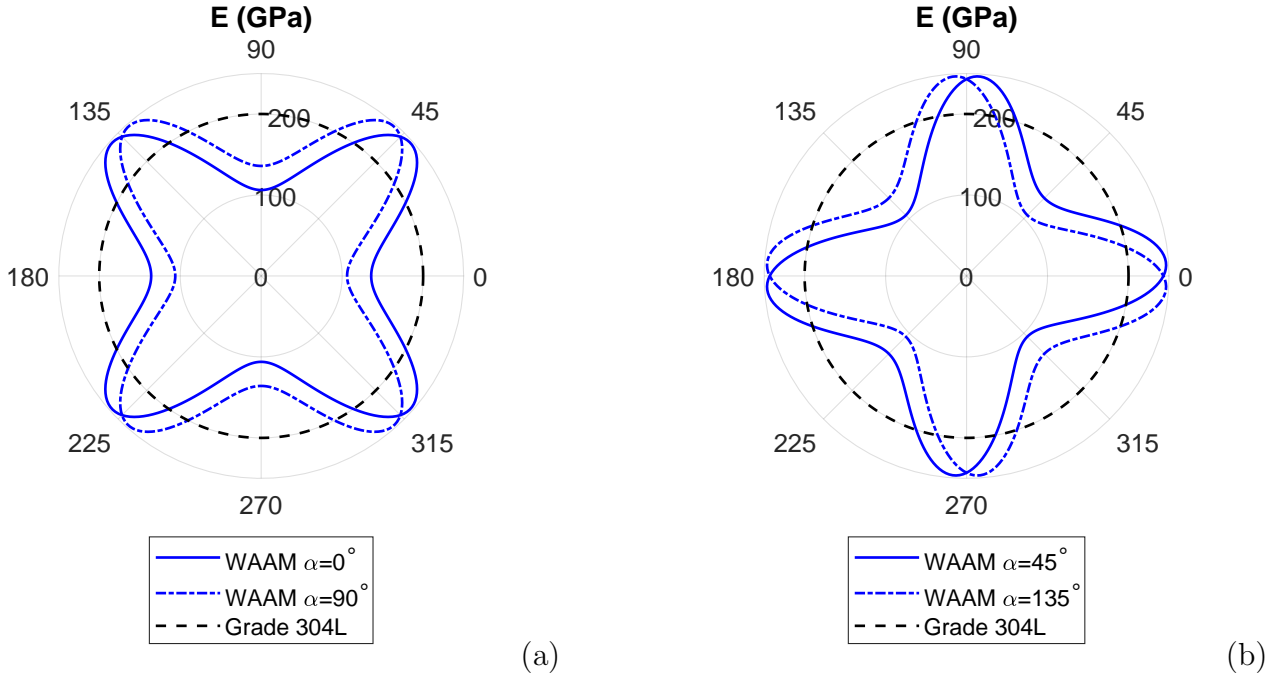
20

Figure 8: Polar plot of the Young's modulus of WAAM-produced stainless steel, for different values of the printing direction: $\alpha = 0°$ and $\alpha = 90°$ (a); $\alpha = 45°$ and $\alpha = 135°$ (b). In each plot, the angular coordinate identifies the direction along which the modulus is given with respect to x_1. The value for Grade 304 stainless steel is drawn for comparison.

values of θ were used to initialize the minimization algorithm when solving Eqn. (11), and the relevant results were compared in terms of both topology and weight. For all the simulations presented next, the tested starting guesses were found not to affect the achieved solutions, except cases admitting specular solutions. When mirrored layouts exist (i.e. solutions with the same weight, but specular topology and specular optimal orientation), convergence to either of them depends on the initialization of the procedure.

4.1. Two-bar trusses

A rectangular domain is considered, with side $50\,\mathrm{cm} \times 150\,\mathrm{cm}$, see Figure 7(a). The specimen is acted upon by a vertical force that is located at the midpoint of the right side, whereas the left
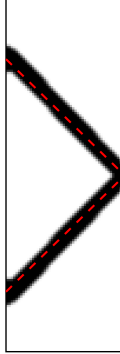
Figure 9: Two-bar truss - Optimal design with isotropic steel, $W = 13.98\%$.

side is fully clamped. $P = 16.67\,\text{kN}$ per mm of thickness of the WAAM-printed plate. The allowed displacement is $u_{lim} = 1\,\text{mm}$. A mesh of 50×150 elements is considered, along with the filter radius $r_{min} = 1.50\,\text{cm}$.

At first, topology optimization for isotropic material is used to find the displacement-constrained optimal layout for Grade 304L stainless steel. At convergence, $u_a = u_{lim}$. This holds for all the simulations run in the numerical section, meaning that the optimal layouts for the same example undergo the same displacement at the loaded node. The well-known two-bar truss is found, see Figure 9. The tie (upper member) and the strut (lower member) are inclined of approximately 45° with respect to the axes of the design domain, which are parallel to x_1 and x_2. The dotted lines in this figure and the subsequent ones mark the 45° directions. The weight at convergence is $W = 13.98\%$ (of the initial design domain).

Then, a topology optimization procedure for orthotropic material is employed to investigate the optimal layouts for the WAAM material with different prescribed printing orientations, see Figure 10. In this figure, and in similar pictures throughout the section, each density map is endowed with a sketch that stands for the printing direction with respect to the relevant optimal solution. Lines stand for the build orientation of the printed layers, i.e. the longitudinal direction of the material
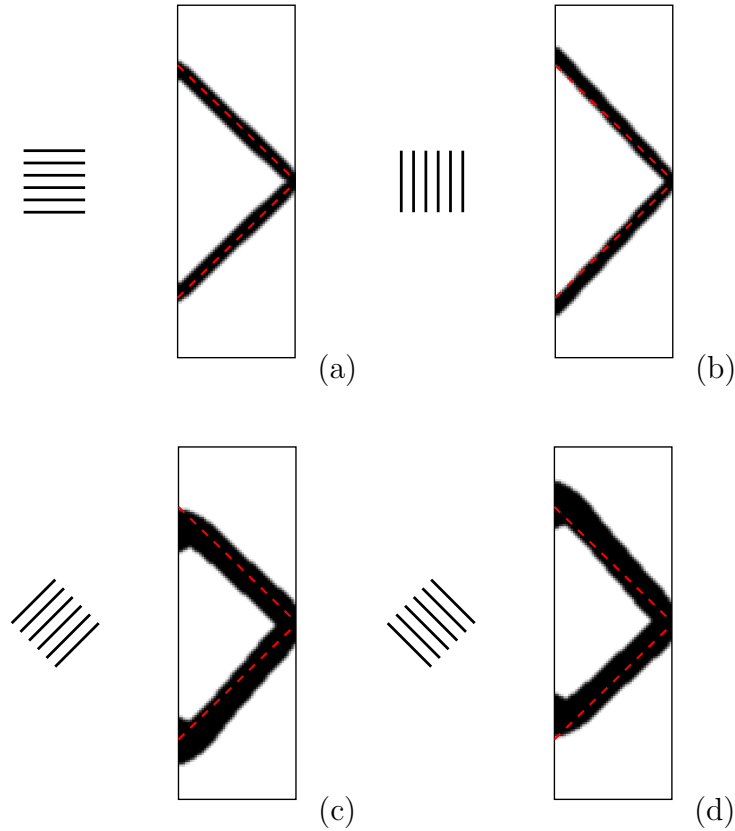
22

Figure 10: Two-bar truss - Optimal design with WAAM material for prescribed printing orientation: $\alpha = 0°$ $W = 11.73\%$ (a), $\alpha = 90°$ $W = 11.67\%$ (b), $\alpha = 45°$ $W = 22.58\%$ (c), $\alpha = 135°$ $W = 22.58\%$ (d).

with respect to the axes of the design domain (see Figure 6). It should be noted that, in order to obtain high quality of the printed parts, the build orientation is normally kept horizontal during the WAAM fabrication process, whereas the part is oriented. Nonetheless, for easy comparisons among different solutions, the axes of the design domain are given the same orientation in all the pictures commented in this section, while the printing direction is oriented accordingly.

In Figure 10(a), the optimal design for $\alpha = 0°$ is presented. The inclined members perfectly match the $45°$ directions and the overall weight is $W = 11.73\%$, around 16% less than the reference design achieved for Grade 304L stainless steel. Indeed, the apparent elastic modulus of the WAAM
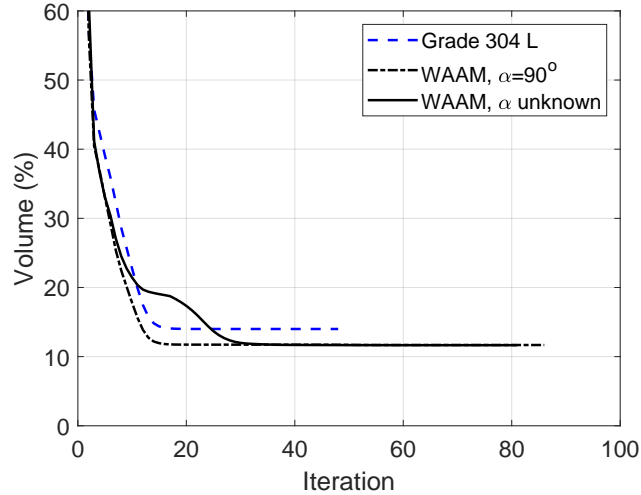
Figure 11: Two-bar truss - Convergence plots for different optimization problems.

material at $\pm 45°$ with respect to x_1, E_D, is 17% higher than the elastic modulus for Grade 304L stainless steel, E_s, see Section 2.2 and Figure 8(a). Figure 10(b) shows the optimal design found for $\alpha = 90°$. The angle between the inclined members is slightly bigger than in the previous cases. According to the equilibrium of the loaded point, the forces in the strut and in the tie increase. Also, the angles between the axis of the inclined members and the longitudinal direction of the material (L) are closer to the values for which the apparent elastic modulus of the WAAM material is equal to E_{max}, see Figure 8(a). While the former issue negatively affects the objective function, the latter is beneficial. Indeed, the overall weight is $W = 11.67\%$, slightly lower than that found for $\alpha = 0°$.

An additional investigation is performed for $\alpha = 45°$, see Figure 10(c). In this case, the symmetry of the design is lost and the weight remarkably increases with respect to the previous solutions. The weight is $W = 22.58\%$, almost twice than the amount of material used for the WAAM material with $\alpha = 90°$, and around 60% bigger than that used in case of isotropic stainless steel. Indeed, the equilibrium requires members that are approximately oriented along the weakest

24

directions of the material, i.e. the longitudinal and the transversal ones. The apparent elastic modulus along these directions is remarkably lower than E_{max} or E_s, see Figure 8(b). According to the equilibrium of the loaded node, the strut is acted upon by a bigger force than the tie, in agreement with the fact that $E_L > E_T$. A mirrored layout is found for $\alpha = 135°$, see Figure 10(d).

The formulation in Eqn. (11) is applied to define, simultaneously, the topology of the material and the printing orientation to achieve the lightest solution. The algorithm detects $\alpha = 90°$ as the best orientation and finds the same optimal solution represented in Figure 10(b). Figure 11 shows convergence plots referring to the conventional procedure of topology optimization for isotropic material (Grade 304L stainless steel), its variation for orthotropic material (WAAM material prescribing $\alpha = 90°$) and the proposed procedure for simultaneous design of topology and printing orientation. Referring to the latter formulation, the curve reported in the plot refers to the starting guess $\theta = 45°$, among the set of initializations points used to test the formulation, i.e. $\theta = 0°, 45°, 90°, 135°$, all of them with the same solution. In this example, the orthotropic modelling requires some additional iterations to find convergence with respect to the isotropic one. The solution of Eqn. (11), accounting for the orientation of the material as an additional variable, calls for 15-20 more iterations to find the final plateau in which minor modifications of the design variables occur.
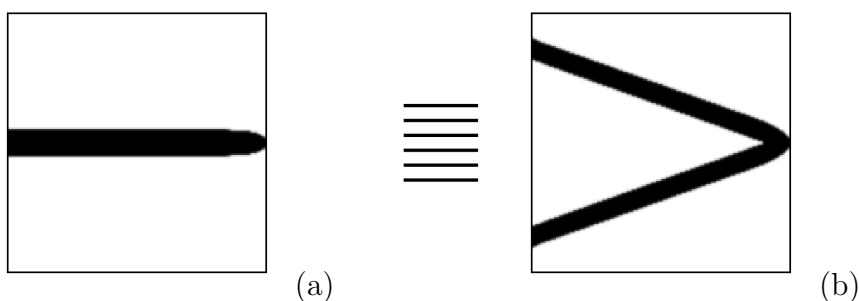

(a)   (b)

Figure 12: Square clamped plate subject to a horizontal force - Optimal design with isotropic steel $W = 10.32\%$ (a) and with WAAM material for prescribed printing orientation $\alpha = 0°$ $W = 15.89\%$ (b)

A variation of the previous example is considered, as represented in Figure 7(b). A square clamped plate with side $150\,\text{cm}$ is loaded by the horizontal force $P = 16.67\,\text{kN}$ (per mm of thickness of the WAAM-printed plate). A mesh of 150×150 elements is considered. The value of u_{lim} and the filter radius are those used in the previous example. The solution for Grade 304L stainless steel is the single tie shown in Figure 12(a), with weight $W = 10.32\%$. A similar layout arises for $\alpha = 45°$ and $\alpha = 135°$, in both cases with weight $W = 8.85\%$, approximately 15% less than the previous solution. Indeed, the elastic modulus of the WAAM-produced material along the horizontal direction, is around 15% bigger than the elastic modulus of isotropic stainless steel E_s, see Figure 8(b). The optimal solutions for $\alpha = 0°$ and $\alpha = 90°$ are different, and consist of two-bar trusses. In the former case $W = 15.89\%$, see Figure 12(b), whereas $W = 20.62\%$ in the latter one. Even though inclined members are longer than a single horizontal tie and call for higher stresses, the elastic modulus along the axes of the inclined bars is much bigger than E_L or E_T, see Section 2.2 and Figure 8(a). The formulation in Eqn. (11) is finally employed to search for the most lightweight material layout using the printing direction as an additional degree of freedom. Two solutions of the type in Figure 12(a) are found depending on the starting orientation, both with $W = 8.71\%$. The optimal orientation of the printed layers is $\alpha = 90° \pm 48.5$, such that the apparent elastic modulus in the horizontal direction is E_{max}, see Section 2.2.

4.2. Cantilever beam

A rectangular domain is considered, with side $80\,\text{cm} \times 40\,\text{cm}$, as shown in Figure 7(c). The specimen is acted upon by a vertical force $P = 8.33\,\text{kN}$ (per mm of thickness of the WAAM-printed plate), which is located at the midpoint of the right side. The left side is fully clamped. The allowed displacement is $u_{lim} = 4\,\text{mm}$. A mesh of 160×80 elements is considered, along with the filter radius $r_{min} = 1.75\,\text{cm}$.

Figure 13(a) shows the displacement-constrained minimum weight design found in case of isotropic stainless steel. The weight at convergence is $W = 36.34\%$. Figure 13(b) shows the
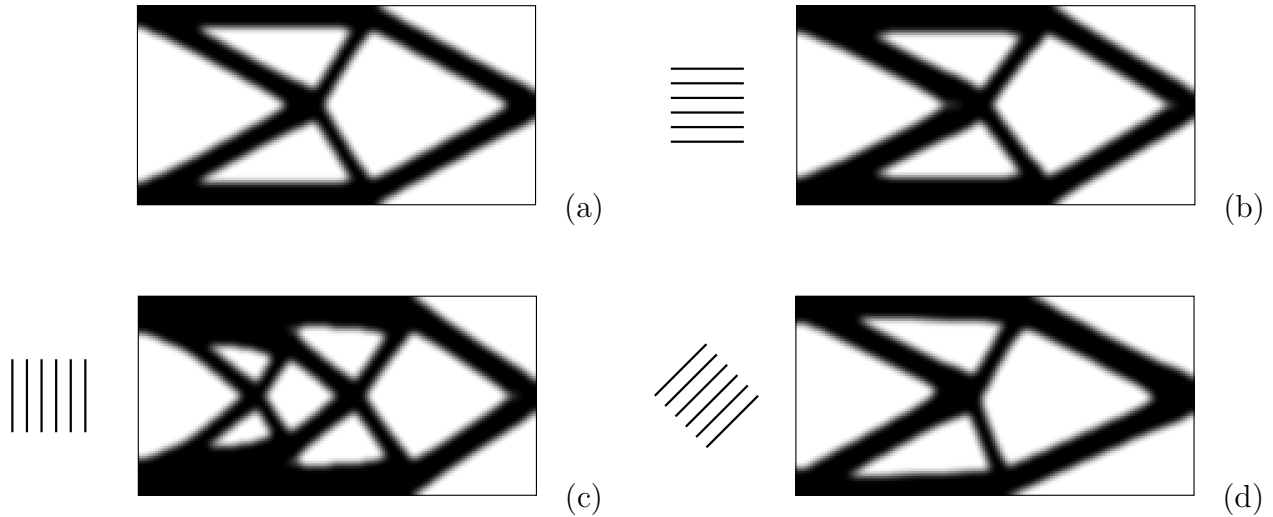
Figure 13: Cantilever beam - Optimal design with isotropic steel $W = 36.34\%$ (a) and with WAAM material for prescribed printing orientation: $\alpha = 0°$ $W = 42.06\%$ (b), $\alpha = 90°$ $W = 51.64\%$ (c), $\alpha = 45°$ $W = 40.52\%$ (d).

optimal solution found for the WAAM material prescribing $\alpha = 0°$. The optimal layout is the same, but the weight increases to $W = 42.06\%$, around 15% more than the reference design. The apparent elastic modulus of the WAAM material in the horizontal direction, E_L, is smaller than the elastic modulus of the Grade 304L stainless steel, E_s, see Figure 8(a). This calls for an increased size of the elements that converge to the clamped side, to limit axial strains and fulfill the enforced displacement constraint. Figure 13(c) shows the optimal solution found for the WAAM material with vertical printing direction, i.e. $\alpha = 90°$. The apparent elastic modulus of the WAAM material in the horizontal direction, E_T, is even smaller than E_L. Hence, the size of the horizontal members remarkably increases with respect to the reference design and a more branched layout is found. The weight at convergence is $W = 51.64\%$, around 40% more than the reference solution found for isotropic stainless steel. A final investigation is performed using WAAM material and $\alpha = 45°$, see Figure 13(d). With this material orientation, the highest value of the apparent elastic modulus is found approximately in the horizontal direction (and in the
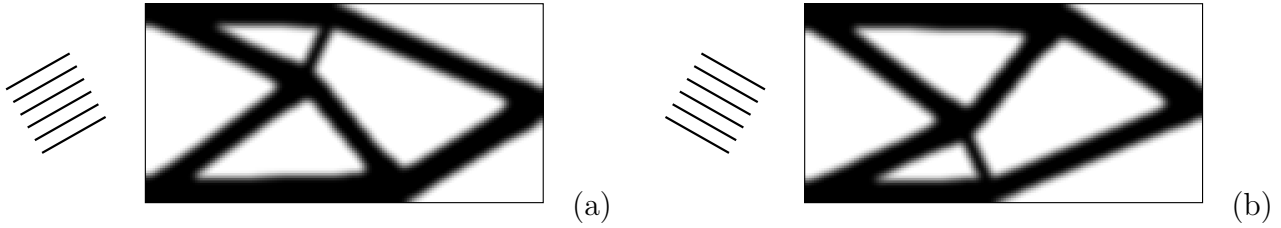
Figure 14: Cantilever beam - Simultaneous design of topology and printing orientation for WAAM material: optimal solutions with computed orientation $\alpha = 29.5°$ $W = 39.58\%$ (a) and $\alpha = 150.5°$ $W = 39.58\%$ (b).

vertical one), whereas smaller ones characterize the other directions, see Figure 8(b). Indeed, the horizontal members of the optimal layout have similar cross-section with respect to the design in Figure 13(a), whereas the other members are generally thicker. A slight lack of symmetry affects the design in Figure 13(d). This is in agreement with the trend of the apparent elastic modulus shown by the polar diagram of Figure 8(b). Indeed, due to the fact that $E_L \neq E_T$, the elastic modulus along any pair of directions that are symmetric with respect to x_1 (or x_2) does not take the same value.A mirrored solution (with respect to the horizontal centroidal axis of the design domain) can be found for $\alpha = 135°$. In both cases, the weight at convergence is $W = 40.52\%$, around 11% more than the reference design.

The formulation in Eqn. (11) is used to seek for a better solution, by introducing the printing orientation as an additional degree of freedom for the minimization procedure. Two mirrored solutions can be found depending on the initial guess used to initialize the optimization, see Figure 14. The weight at convergence is $W = 39.58\%$, only 9% more than the reference design. The orientation of the material is $\alpha = 90° \pm 60.5$. It must be remarked that the lack of symmetry is much more evident than in Figure 13(d). Indeed, the orientation of the printed material is such that the elastic modulus along any pair of symmetric directions with respect to x_1 (or x_2) takes values that can be very different from each other, see Figure 15.

In Figure 16 a comparison of the reference optimal design for isotropic steel (blue dotted line)
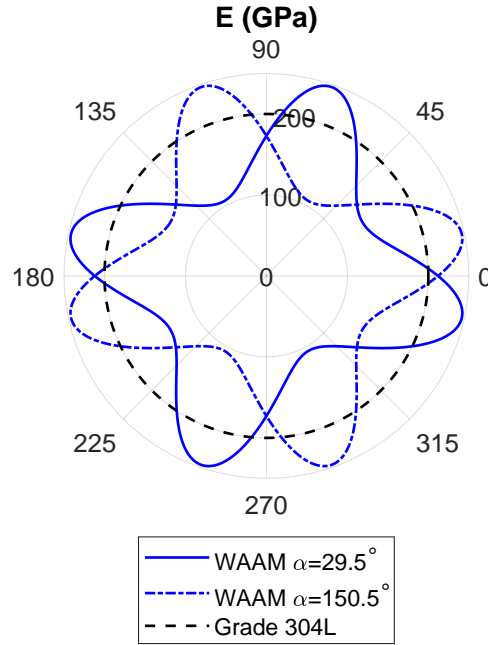
Figure 15: Polar plot of the Young's modulus of WAAM-produced stainless steel for $\alpha = 29.5°$ and $\alpha = 150.5°$. The angular coordinate identifies the direction along which the modulus is given with respect to x_1. The value for Grade 304 stainless steel is drawn for comparison.

vs one of the achieved optimal layouts for the WAAM material (red line, $\alpha = 150.5°$) is provided, by overlapping the isolines $\tilde{\rho} = 0.5$ of the relevant density maps. With respect to the reference design, minor changes are found in terms of cross section, whereas the major difference lies upon the position of the three unrestrained and unloaded nodes of the truss-like structure, with a consequent re-orientation of its members.

4.3. Simply-supported beam

A rectangular domain is considered, with side $160 \, \text{cm} \times 40 \, \text{cm}$, see Figure 7(d). The specimen is acted upon by a vertical force $P = 6.66 \, \text{kN}$ (per mm of thickness) that is located at the midpoint of the upper side, whereas it is simply supported at the extreme points of the lower side. The
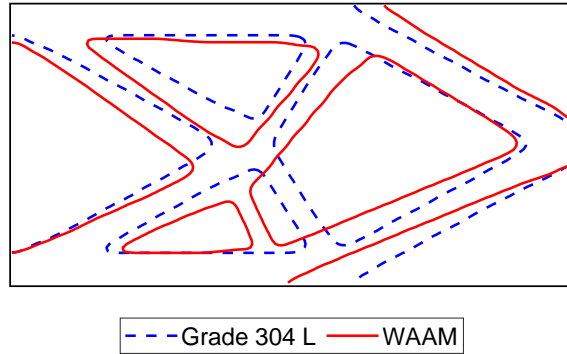
Figure 16: Cantilever beam - Optimal design for isotropic steel (blue dotted line) vs optimal design for WAAM material (red line).

allowed displacement is $u_{lim} = 1\,\text{mm}$. A mesh with 320×80 elements is used, along with the filter radius $r_{min} = 2.50\,\text{cm}$.

Figure 17(a) shows the displacement-constrained minimum weight solution found for Grade 304L stainless steel. The optimal design is a truss-like structure whose top chord is arcuated. The weight at convergence is $W = 37.96\%$. Figure 17(b) and (c) show the optimal layouts found in case of WAAM material with $\alpha = 0°$ ($W = 45.21\%$) and $\alpha = 90°$ ($W = 51.02\%$), respectively. The number of elements is the same than in the reference solution, but the top chord becomes horizontal. This allows increasing the inner lever arm, i.e. the distance of forces in the tensile and compression chord, in the vicinity of the central region of the specimen. Also, the elements of both chords are thicker with respect to the reference solution. This is mainly due to the fact that the elastic modulus of the traditional stainless steel, E_s, is larger than the apparent elastic modulus of the WAAM material in the horizontal direction, i.e. E_L and E_T for $\alpha = 0°$ and $\alpha = 90°$ respectively, see Figure 8(a). The former layout is 19% heavier than the reference solution, whereas the latter is 34% heavier. The weight increase with respect to the isotropic solution can be reduced by prescribing material orientations of $\alpha = 90° \pm 45°$. Figure 17(d) refers to the optimal solution found for $\alpha = 45°$, which weights $W = 41.93\%$, only 10% more than the reference design. A
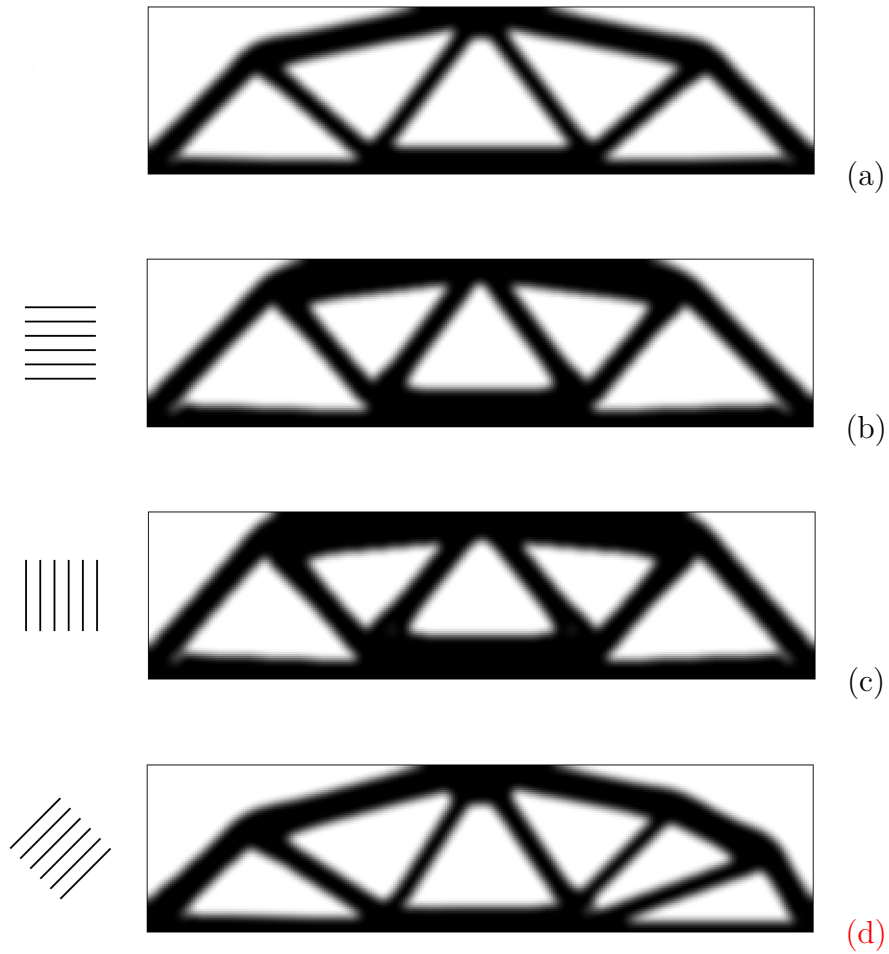
Figure 17: Simply-supported beam - Optimal design with isotropic steel $W = 37.96\%$ (a) and with WAAM material for prescribed printing orientation: $\alpha = 0°$ $W = 45.21\%$ (b), $\alpha = 90°$ $W = 51.02\%$ (c), $\alpha = 45°$ $W = 41.93\%$ (d).

mirrored solution (with respect to the vertical centroidal axis of the design domain) can be found for $\alpha = 135°$. The symmetry observed in the previous solutions is lost, accordingly to the variation of the apparent elastic modulus shown by the polar diagrams of Figure 8(b). For $\alpha = 90° \pm 45°$, the top chord has an arch-like shape, as in case of isotropic material, see Figure 17(a). However, half of the design domain has a greater number of elements in this chord, as well as diagonal members.
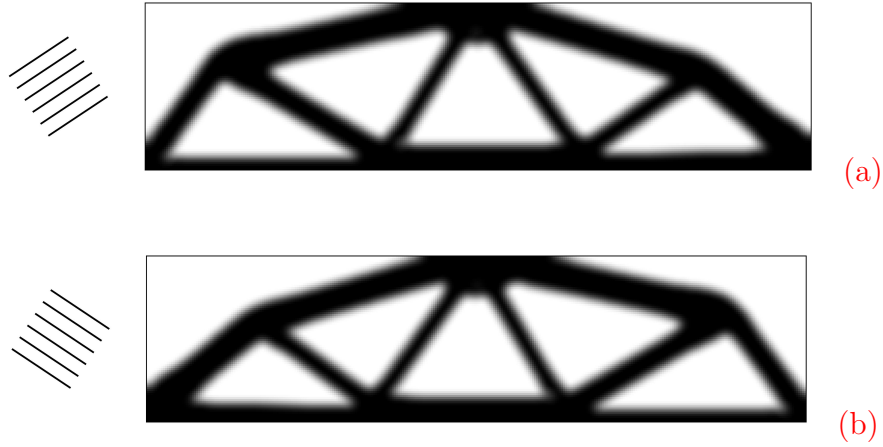
Figure 18: Simply-supported beam - Simultaneous design of topology and printing orientation for WAAM material: optimal solution with computed orientation $\alpha = 33.5°$ $W = 41.09\%$ (a) and $\alpha = 146.5°$ $W = 41.09\%$ (b).

An additional investigation is performed using the WAAM material to search for a lighter design with respect to the solution found for $\alpha = 90° \pm 45°$. The formulation in Eqn. (11) detects minimum weight solutions for $\alpha = 90° \pm 56.5°$. The weight at convergence is $W = 41.09\%$ in both cases, slightly less than that of the solution in Figure 17(d) (and around 8% more than that of the reference design with Grade 304L stainless steel). The achieved (specular) optimal solutions are shown in Figure 18. A comparison of the optimal design found for $\alpha = 146.5°$ with respect to the reference optimal design for isotropic stainless steel is given in Figure 19. The isolines $\tilde{\rho} = 0.5$ of the relevant density maps are overlapped, the red lines referring to the former design and the blue dotted lines to the latter. Notwithstanding the lack of symmetry which is related to the anisotropy of the WAAM material, the optimal solutions are quite similar with respect to the topology. They differ slightly in terms of size of the members and for the coordinates of the unrestrained and unloaded nodes of the truss (especially those belonging to the top chord).

The formulation for simultaneous design of distribution and orientation of the WAAM-produced material is finally used to investigate optimal solutions in case of stricter requirements on the
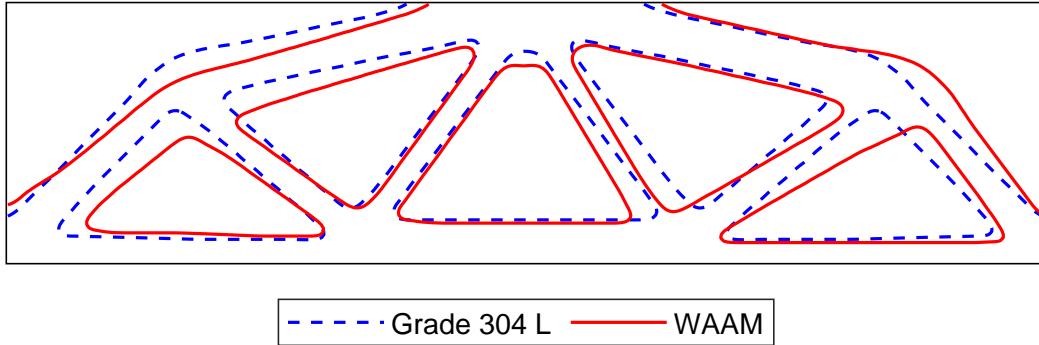
Figure 19: Simply-supported beam - Optimal design for isotropic steel (blue dotted line) vs optimal design for WAAM material (red line).

allowed displacement.

Figure 20(a) shows one of the two specular layouts found for $u_{lim} = 0.75$ mm. The computed orientations are $\alpha = 90° \pm 54.5°$, only $\pm 2°$ with respect to the optimal values found for $u_{lim} = 1$ mm. Indeed, the optimal design consists of a heavier version of the topology presented in Figure 18(b).

Figure 20(b) shows one of the two specular layouts found for $u_{lim} = 0.60$ mm. A more branched (and heavier) layout is found at convergence, including a re-arrangement of many members (both in the top chord and in the webs). The computed optimal orientations of the printed layers are $\alpha = 90° \pm 48.5°$, approximately $\pm 8°$ with respect to the values found for $u_{lim} = 1$ mm. Hence, the observed change in geometry happens in conjunction with a not negligible re-orientation of the printed layers.

5. Conclusions and ongoing research

This work addresses the optimal design of stiff structural parts to be fabricated by Wire-and-Arc Additive Manufacturing (WAAM), taking into account the peculiar anisotropic structural response of this layered material.
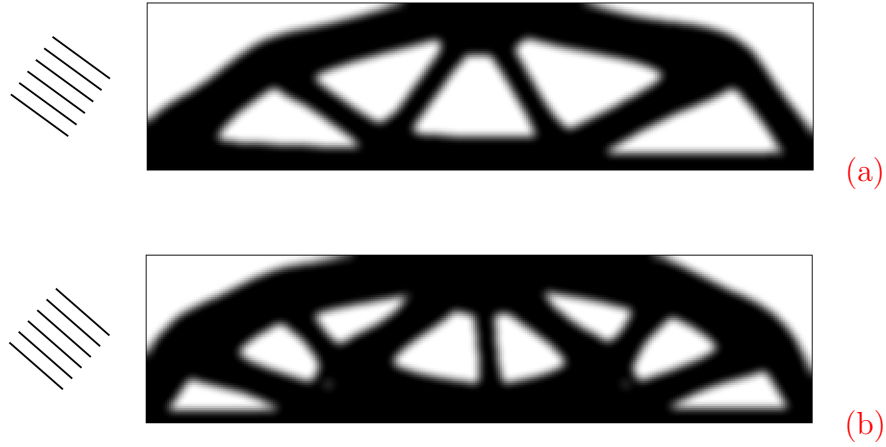
Figure 20: Simply-supported beam - Simultaneous design of topology and printing orientation for WAAM material: optimal solution for $u_{lim} = 0.75\,\text{mm}$ with computed orientation $\alpha = 144.5°$ $W = 53.63\%$ (a) and optimal solution for $u_{lim} = 0.60\,\text{mm}$ with computed orientation $\alpha = 138.5°$ $W = 69.14\%$ (b).

An orthotropic model is adopted to process data from experimental tests reported in the recent literature, thus deriving the compliance tensor of the printed material in its symmetry axes (the longitudinal and transversal directions). At first, a SIMP-based approach is implemented to deal with the optimal distribution of this orthotropic phase, given the material orientation (which is the printing direction). A displacement-constrained minimum weight problem is considered, with the aim of comparing the weight of specimens designed to meet the same requirement at the serviceability limit state. Hence, a formulation for the simultaneous design of the topology and of the build direction, which is assumed to remain the same during the whole printing process of the part, is proposed. To this goal, the material orientation is embedded in the formulation as an additional degree of freedom with respect to the field of the material density. Mathematical programming is adopted to solve the minimization problem. The sensitivity analysis is performed through the adjoint method so that only two linear systems are solved per iteration to evaluate constraints and their sensitivities.

The optimization for WAAM material with prescribed printing orientations reveals different

topologies with respect to that achieved for the isotropic reference case. A remarkable variability in terms of weight and geometry of the optimal solutions is reported, depending on the prescribed orientation. The proposed formulation for the simultaneous optimization of topology and orientation of the WAAM material allows finding optimal solutions that are only a few percent heavier than the reference solution with Grade 304L stainless steel. A reduction in terms of weight is obtained not only through a suitable orientation of the material but also in conjunction with modifications of the topology. Asymmetries may arise in the optimal layouts, due to the anisotropy of the material behaviour.

The proposed tools can be conveniently used to save weight in the WAAM process by customizing optimal solutions for any design domain, load conditions and restraint configurations. The proposed approach is a computationally efficient energy-based procedure. Due to the adoption of mathematical programming, other enforcements could be effectively implemented within the considered displacement-constrained formulation for orthotropic materials, such as buckling constraints and stress constraints. These aspects are currently under investigation.

References

[1] Addis W. Building: 3000 years of design engineering and construction. Phaidon 2007.

[2] Carpo M. The digital turn in architecture 1992-2012. John Wiley and Sons 2013.

[3] Adriaenssens S, Block P, Veenendaal D, Williams C. Shell structures for architecture: form finding and optimization. Routledge 2014.

[4] Bruggi M. A constrained force density method for the funicular analysis and design of arches, domes and vaults. Int J Solids Struct 2020;193-194:251-269.

[5] Attaran M. The rise of 3-D printing: The advantages of additive manufacturing over traditional manufacturing. Bus Horiz 2017;60(5):677-688.

[6] Thomas CL, Gaffney TM, Kaza S, Lee CH, Rapid prototyping of large scale aerospace structures. IEEE Aerospace Applications Conference Proceedings; 1996.

[7] Frazier WE. Metal Additive Manufacturing: A Review. J. of Materi Eng and Perform 2014; 23: 1917-1928.

[8] Wu B, Pan Z, Ding D, Cuiuri D, Li H, Xu J, et al. A review of the wire arc additive manufacturing of metals: properties, defects and quality improvement. J Manuf Processes 2018;35:127-139.

[9] Buchanan C, Gardner L. Metal 3D printing in construction: A review of methods, research, applications, opportunities and challenges. Eng Struct 2019;180:332-348.

[10] Dinovitzer M, Chen X, Laliberte J, Huang X, Frei H. Effect of wire and arc additive manufacturing (WAAM) process parameters on bead geometry and microstructure. Addit Manuf 2019;26:138-146.

[11] Xu X, Ganguly S, Ding J, Guo S, Williams S, Martina F. Microstructural evolution and mechanical properties of maraging steel produced by wire + arc additive manufacture process. Mater Charact 2018;143:152-162.

[12] Ge J, Lin J, Chen Y, Lei Y, Fu H. Characterization of wire arc additive manufacturing 2Cr13 part: Process stability, microstructural evolution, and tensile properties. J Alloys Compd 2018;748:911-921.

[13] Gordon JV, Haden CV, Nied HF, Vinci RP, Harlow DG. Fatigue crack growth anisotropy, texture and residual stress in austenitic steel made by wire and arc additive manufacturing. Mater Sci Eng A 2018;724:431-438.

[14] Ji L, Lu J, Liu C, Jing C, Fan H, Ma S. Microstructure and mechanical properties of 304L steel fabricated by arc additive manufacturing. MATEC Web of Conferences; 2017.

[15] Haden CV, Zeng G, Carter FM, Ruhl C, Krick BA, Harlow DG. Wire and arc additive manufactured steel: Tensile and wear properties. Addit Manuf 2017;16:115-123.

[16] Laghi V, Palermo M, Gasparini G, Girelli VA, Trombetti T. Experimental results for structural design of Wire-and-Arc Additive Manufactured stainless steel members. J Constr Steel Res 2019.

[17] Laghi V, Palermo M, Tonelli L, Gasparini G, Ceschini L, Trombetti T. Tensile properties and microstructural features of 304L austenitic stainless steel produced by wire-and-arc additive manufacturing. Int J Adv Manuf Technol 2020;106(9-10):3693-3705.

[18] Laghi V, Palermo M, Gasparini G, Girelli VA, Trombetti T. Mechanical influence of the surface roughness on Wire-and-Arc Additively Manufactured planar elements. Journal of Constructional Steel Research, under review.

[19] Bendsøe MP, Kikuchi N. Generating optimal topologies in structural design using a homogenization method. Comput Methods Appl Mech Eng 1988;71(2):197-224.

[20] Zhang W, Zhu J, Gao T. Topology Optimization in Engineering Structure Design. Topology Optimization in Engineering Structure Design; 2016. p. 1-294.

[21] Bendsøe MP, Sigmund O. Topology Optimization: Theory, Methods and Applications. Springer 2003.

[22] Sigmund O, Maute K. Topology optimization approaches: A comparative review. Struct Multidiscip Opt 2013;48(6):1031-1055

[23] Liu J, Gaynor AT, Chen S, Kang Z, Suresh K, Takezawa A, et al. Current and future trends in topology optimization for additive manufacturing. Struct Multidiscip Opt 2018;57(6):2457-2483.

[24] Meng L, Zhang W, Quan D, Shi G, Tang L, Hou Y, et al. From Topology Optimization Design to Additive Manufacturing: Today's Success and Tomorrow's Roadmap. Arch Comput Methods Eng 2019.

[25] Allaire G, Bogosel B. Optimizing supports for additive manufacturing. Struct Multidiscip Opt 2018;58(6):2493-2515

[26] Bruggi M, Parolini N, Regazzoni F, Verani M. Topology optimization with a time-integral cost functional. Finite Elem Anal Des 2018;140:11-22.

[27] Allaire G, Dapogny C, Estevez R, Faure A, Michailidis G. Structural optimization under overhang constraints imposed by additive manufacturing technologies. J Comput Phys 2017;351:295-328.

[28] Amir O, Mass Y. Topology optimization for staged construction. Struct Multidiscip Opt 2018;57(4):1679-1694.

[29] Guo X, Zhou J, Zhang W, Du Z, Liu C, Liu Y. Self-supporting structure design in additive manufacturing through explicit topology optimization. Comput Methods Appl Mech Eng 2017;323:27-63.

[30] Langelaar M. Combined optimization of part topology, support structure layout and build orientation for additive manufacturing. Struct Multidiscip Opt 2018;57(5):1985-2004.

[31] Wang W, Munro D, Wang CCL, van Keulen F, Wu J. Space-time topology optimization for additive manufacturing: Concurrent optimization of structural layout and fabrication sequence. Struct Multidiscip Opt 2020;61(1).

[32] Groen JP, Sigmund O. Homogenization-based topology optimization for high-resolution manufacturable microstructures. Int J Numer Methods Eng 2018;113(8):1148-1163.

[33] Allaire G, Geoffroy-Donders P, Pantz O. Topology optimization of modulated and oriented periodic microstructures by the homogenization method. Comput Math Appl 2019;78(7):2197-2229

[34] Nikbakt S, Kamarian S, Shakeri M. A review on optimization of composite structures Part I: Laminated composites. Compos Struct 2018;195:158-185.

[35] Achtziger W, Topology Optimization of Discrete Structures. In: Rozvany G.I.N. (eds) Topology Optimization in Structural Mechanics. International Centre for Mechanical Sciences (Courses and Lectures). Vol 374. Vienna: Springer 1997.

[36] Nomura T, Dede EM, Lee J, Yamasaki S, Matsumori T, Kawamoto A, et al. General topology optimization method with continuous and discrete orientation design using isoparametric projection. Int J Numer Methods Eng 2015;101(8):571-605.

[37] Peeters D, van Baalen D, Abdallah M. Combining topology and lamination parameter optimisation. Struct Multidiscip Opt 2015;52(1):105-120

[38] Bruggi M, Taliercio A. Optimal strengthening of concrete plates with unidirectional fiber-reinforcing layers. Int J Solids Struct 2015;67-68:311-325.

[39] Lee JW, Kim JJ, Yoon GH. Stress constraint topology optimization using layerwise theory for composite laminates. Compos Struct 2019;226

[40] Lee JW, Kim JJ, Kim HS, Yoon GH. Application of a layerwise theory for efficient topology optimization of laminate structure. J Mech Sci Technol 2019;33(2):711-719

[41] Ranaivomiarana N, Irisarri F-, Bettebghor D, Desmorat B. Concurrent optimization of material spatial distribution and material anisotropy repartition for two-dimensional structures. Continuum Mech Thermodyn 2019;31(1):133-146

[42] Vannucci P. Plane anisotropy by the polar method. Meccanica 2005;40(4-6 SPEC. ISS.):437-454.

[43] Laghi V, Palermo M, Gasparini G, Girelli VA, Trombetti T. Geometrical Characterization Of Wire-And-Arc Additive Manufactured Steel Element. Adv. Mater 2019; 10(10): 695-699.

[44] European Committee for Standardization CEN (2015) EN 1993-1-4:2006+a1:2015 Eurocode 3 Design of Steel Structures, Part 1-4: General Rules Supplementary Rules for Stainless Steel.

[45] Kyvelou P, Slack H, Daskalaki Mountanou D, Wadee MA, Britton TB, Buchanan C, et al. Mechanical and microstructural testing of wire and arc additively manufactured sheet material. Mater Des 2020;192.

[46] Kau A K. Mechanics of Composite Materials. Boca Raton: CRC Press 2006.

[47] Vannucci P. Anisotropic Elasticity. Lecture Notes in Applied and Computational Mechanics book series. Vol 85. Heidelberg: Springer International Publishing 2018.

[48] Briccola D, Bruggi M. Analysis of 3D linear elastic masonry-like structures through the API of a finite element software. Adv Eng Software 2019;133:60-75.

[49] Borrvall T, Petersson J. Topology optimization using regularized intermediate density control. Comput Methods Appl Mech Eng 2001;190(37-38):4911-4928.

[50] Bourdin B. Filters in topology optimization. Int J Numer Methods Eng 2001;50(9):2143-2158.

[51] Wang F, Lazarov B, Sigmund O. On projection methods, convergence and robust formulations in topology optimization. Struct Multidiscip Optim 2011; 43(6):767-784

[52] Langelaar M. An additive manufacturing filter for topology optimization of print-ready designs. Struct Multidiscip Opt 2017;55(3):871-883.

[53] Svanberg K. Method of moving asymptotes - A new method for structural optimization. Int J Numer Methods Eng 1987;24(2):359-373.